Egypt. J. Chem. **Vol. 68**, No. 11 pp. 441 - 454 (2025)

Egyptian Journal of Chemistry

http://ejchem.journals.ekb.eg/

Comparative studies on Cr(VI) ions by reduced graphene oxide and SBA-16 mesoporous silica and their composites with Cu-MOF

Khadiga M. Abas[a], Ghada M. Mohamed[a], Sohair A. Sayed Ahmed[a], Nady A. Fathy[a]*, Alaa S. Abdelmoaty[b],

[a)] Physical Chemistry Department, [b)]Inorganic Chemistry Department, Advanced Materials Technology and Mineral Resources Research Institute, National Research Centre, 33 EL Buhouth St., Dokki, Cairo, P.O. 12622, Egypt.

Abstract

This work examines the adsorption performance of novel adsorbents such as reduced graphene oxide (GO) and mesoporous silica (SBA-16) which synthesized from rice husk ash, and then composited with Cu-metal organic framework (Cu-MOF) for the first time. XRD, FTIR, EDX, FE-SEM and N_2 adsorption techniques were studied. The adsorption performance of investigated adsorbents toward removal of hexavalent chromium (Cr(VI)) ions was carried out as a function of pH and initial concentration of Cr(VI) ions. The obtained GO and SBA-16 samples exhibited a superior porosity than that of Cu-MOF, Cu-MOF/GO and Cu-MOF/SBA-16 that owed to close of internal pores in both GO and SBA-16 samples upon loading Cu-MOF particles. The Langmuir and Temkin models prescribed Cr(VI) adsorption more accurately. The maximum adsorption capacity of Cr(VI) was 86.1 mg/g by GO while 77 and 66.7 mg/g by Cu-MOF/GO and Cu-MOF/SBA-16, respectively. The adsorption Cr(VI) mechanism followed the pseudo-first order kinetic model. Therefore, the as-prepared GO and SBA-16 derived from rice husk ash and their composites with Cu-MOF can candidate as effective adsorbents for removal of Cr(IV) ions from their aqueous media.

Keywords*:* Rice husk ash, reduced graphene oxide, SBA-16, Cu-MOF, chromium (VI), adsorption

1. Introduction

The increase in agricultural production, population, and industrialization is causing major environmental issues such as waste accumulation and water contamination. Hence, the biggest difficulty challenge facing scientists and environmentalists is the management of industrial and agricultural wastes as well as contaminated water streams to provide a safe, sustainable environment and healthy living for people. Water contamination is a global issue resulting in an estimated 14,000 people dying every day due to organic, inorganic, biological, or radioactive wastes [1]. Specifically, nickel, copper, zinc, cadmium, and lead hexavalent chromium (Cr, VI) are categorized as common and strong toxic inorganic pollutants in wastewater [2]. Because of the high toxic level of Cr (VI) in soil and water resulting in both natural and man-made processes, environmental contamination of this element is gaining more attention worldwide [3-6]. There are several chromium-containing processes like mining, steel and metal alloy fabrication, paint manufacturing, tannery, wood, paper and dye processing that would increase the chromium levels in wastewater [5, 6]. Cr (VI) is mostly formed hexavalent forms (e.g., Cr2O72–, HCr2O7– or HCrO4–) which are harmful to humans and environment. It has been reported that human dangers from Cr(VI) ranged from skin irritation to DNA damage and cancer formation, depending on the dosage, exposure level, and length of time [6]. Currently, a variety of technologies are applied to eradicate Cr (VI) ions from water such as chemical reduction, photocatalytic, photo-Fenton oxidation, ultrasound, electro-coagulation, flocculation, chemical precipitation, ozonation, aerobic degradation, bioremediation and adsorption [6–10] to reach the admissible discharge limits of Cr (VI) between 0.05 and 5 mg/L[5].

Among these methods, the adsorption using amazing adsorbents is one of the finest strategies for water pollution cleanup because it is simpler, ecofriendly, affordable and efficient route. Cr(VI) adsorption has been investigated by studying factors such as the nature, surface property and modification of adsorbent, beside other experimental parameters (e.g., contact time, pH and initial Cr(VI) concentration, ionic strength, etc.) to improve the adsorption process [10]. However, Cr(VI) adsorption greatly relied on pH as Cr(VI) adsorbed heavily from its acidic solutions but little to no adsorption under alkaline pH due to formation of its anionic species [10–18]. In this context, porous adsorbents such as activated carbons, carbon nanostructures such as carbon nanotubes and graphene derivatives, metal loaded chars, zeolite, metal-organic frameworks (MOFs) and magnetic composites were effectively performed as Cr(VI)-adsorbents [10–18]. Metal-organic frameworks (MOFs) nanostructures are currently attracting a lot of interest from both the academic and industrial worlds because of their unique contributions to medicine, remote sensing, wastewater treatment, air purification, and renewable energy sources [7].

*Corresponding author e-mail: fathyna.77@hotmail.com , (Nady A.Fathy)
.Receive Date: 03 March 2025, Revise Date:, Accept Date: 07 April 2025
DOI:10.21608/ejchem.2025.365156.11383

Shao et al. [16] investigated the adsorption of Cr(VI) onto Cu(II)-MOF confirming that the adsorption capacity of Cr(VI) about 190 mg/g is controlled by single crystal-single crystal coordination substitution process between HCrO4- and Cu(II)-MOF. Furthermore, compared to other MOFs, Cu (II)-MOF is easier to produce on a large scale and has a high water stability, making it appropriate for water treatment applications [16].

Particularly, agricultural wastes are inexpensive materials and recently utilized for producing smart adsorbents in the last decades [19-25]. Rice husks waste is one of the by-products of rice production containing valuable silica (SiO2) and carbonaceous materials for creating ecofriendly and economic materials used in treatment of the environment issues[19, 20]. Lately, some investigations have been carried out to utilize rice silica-containing rice husk ashes in preparing silica and ordered mesoporous silica (e.g., SBA-15, SBA-16 and MCM-22) using copolymer surfactants in acidic medium[19–23]. On the other hand, carbon-containing rice husk is a promising carbonaceous precursor for preparing carbon-based nanomaterials[19]. Liou and Wang [24] employed the activation of rice husk ashless with ZnCl2 and H3PO4 to generate activated carbons, and then made composites of those with graphene oxide (GO) fabricated from graphite using a modified Hummers process [24]. In another work, rice husk ash (RHA) and potassium hydroxide (KOH) and in a mass ratio of 1: 5 were carbonized at 900 oC for two hours to create few layer graphene [25].

The combination of Cu-MOF with GO and SBA-16 materials derived from RHA as novel adsorbents maybe proposed to solve the recovery and aggregation shortcomings of GO, SBA-16 or Cu-MOF alone during the liquid-adsorption process. However, to author's knowledge, the suggested investigation of preparing such adsorbents in the current work for removal of Cr(VI) has not examined yet. Accordingly, the construction Cu-MOF into the surface of both GO and SBA-16 derived from RHA through a physical mixing in presence of a Schiff base cross-linker called 3-aminopropyl triethoxysilane (APTES) as novel adsorbents for Cr(VI) is not studied also. In this study, APTES is used as a cross-linker to functionalize the surface of both GO and SBA-16 because of its available nitrogen sites and silanol moieties which are favorable for the covalent attachment of their functional groups with Cu-MOF. Therefore, comparative studies on the adsorption of Cr(VI) by the as-prepared adsorbents were examined during kinetic and adsorption studies. The resulting crystal phases, functional surface groups, elemental composition, total porosity and morphology of the prepared samples were identified by X-ray diffraction (XRD), Fourier transform infrared spectroscopy (FTIR), energy-dispersive X-ray spectroscopy (EDX), field emission-scanning electron microscope (FE-SEM) and N2 adsorption analysis at -196oC. Equilibrium, kinetic and thermodynamic Cr(VI) adsorption studies were demonstrated using various models to explore the mechanism of adsorption.

2. Materials and methods

2.1. Materials

Rice husks were collected from local farms in Delta region of Egypt. Sodium hydroxide pellets (NaOH, 98%), potassium hydroxide (KOH, 98%), hydrochloric acid (HCl, 37%) and ethanol (CH3CH2OH, 99%) were obtained from Alpha-Chemika. Toluene liquid ($C_6H_5CH_3$, 99%) was supplied from ADWIC Company. Pluronic F127 triblock copolymer (EO106PO70EO106, 99%) and 3-Aminopropyl triethoxysilane (H2N(CH2)3Si(OC2H5)3, Mw=221.37 g/mol) labelled as APTES were purchased from Sigma-Aldrich. Distilled water and analytical grade water were utilized just as is, without any additional purification.

2.2. Preparation of mesoporous silica and graphene oxide

Primarily three steps were included to prepare the precursors, i.e., sodium silicate and activated carbon used in preparation of mesoporous silica (SBA-16) and graphene oxide (GO), respectively. Accordingly after purifying and sieving rice husks, (i) the rice husk ash (RHA) was obtained from powdered rice husk through carbonization at 500 oC for 2 h followed by leaching with 1M HCl solution. (ii) To extract sodium silicate solution from RHA, the produced RHA was treated with 0.5 M NaOH solution at 90 oC for 2 h, knowing as a desiliconization process. The resulting sodium silicate was mixed with F127 copolymer and 2 M HCl solution then hydrothermal treatment was performed at 100 oC for 48 h followed by the calcination at 550 oC for 4 h to prepare SBA-16 as prescribed formerly [22]. (iii) The remaining carbon of RHA ashless was mixed with KOH pellets using little water in a mass ratio 1:3, subsequently activation at 650 oC for 2 h under N2 gas flow. The obtained activated carbon was chemically oxidized using modified Tour method to prepare graphene oxide (GO) as described previously [26].

2.3. Preparation of Cu-MOF composites

The studied Cu-MOF was prepared formerly from terephthalic acid (H2BDC), copper nitrate trihydrate with melamine during hydrothermal method using Teflon-lined stainless steel autoclave at 100 oC for 36 h as reported elsewhere [27]. Herein, two composites from Cu-MOF/SBA-16 and Cu-MOF/GO were obtained using APTES as an organosilane cross-linker. About 500 mg GO (or SBA-16) was dispersed in 50 mL of toluene and 50 mL of ethanol during sonication for 1 h at 40 oC. Then, 4ml of APTES was added to the above GO solution under mechanical stirring for 20 min. Following, 50 mg of Cu-MOF was added and all mixture refluxed at 90 oC for 2 h. After cooling, the resulting composites were washed thoroughly with distilled water and ethanol until pH=6.0 and dried overnight at 60 oC to obtain Cu-MOF/GO and Cu-MOF/SBA-16 samples.

2.4. Samples characterization

The main crystallite phases of samples were detected by a X-ray diffraction (XRD) diffractometer (Bruker D8 Advance, Germany) with CuKα1 (λ=0.15418 nm) at room temperature with monochromator settings at 40 kV and 40 mA. Fourier transform infrared spectroscopy (FTIR) spectra of samples were recorded using a KBr pressed disc to provide the principal functional groups using an FTIR 6500 spectrometer (JASCO, Japan) in the 400-4000 cm-1 range. The morphology of the produced samples was assessed using a field emission-scanning electron microscope (FE-SEM, FEI Quanta FEG-250) combined with energy-dispersive X-ray spectroscopy (EDX) to record the element composition. Textural parameters such as Brunauer-Emmett-Teller (BET) surface area (SBET, m2/g), total pore volume (VP, cm3/g), and average pore diameter (RP,

nm) were determined using nitrogen adsorption at -196oC (BEL-Sorp-max, Microtrac Bel Crop, Japan). Prior to N2 adsorption run, the samples were outgassed under a pressure at 150°C for 12 h. In addition, the pore size distributions in the samples were detected using non-local density functional theory (NLDFT) model.

2.5. Adsorption experiments

A stock solution of K2Cr2O7 (1000 mg/L) was generated by dissolving 2.8 g in 1 L of distilled water and then diluted to required initial concentrations (Co= 20-100mg/L). The as-prepared GO, SBA-16, Cu-MOF, Cu-MOF/GO and Cu-MOF/SBA-16 adsorbents were tested for studying the adsorption behavior of Cr(VI) in a static adsorption mode under different conditions. About 0.02 g of the prepared samples were conducted with 20 mL of Cr (VI) (Co=50 mg/L) at varied pHs of 2, 3 and 5 at 25oC under shaking at 220 rpm for 2h to reach equilibrium in order to evaluate the impact of pH. The pH was adjusted using either 0.1 M solution of NaOH or HCl. For kinetic studies, about 0.05 g of the obtained samples were mixed with 50 mL of Cr (VI) (Co= 50 mg/L) at the optimum pH=2 under shaking at 220 rpm during contact time (0-180 min). Adsorption isotherms were achieved by conducting 0.02 g of the prepared samples with 20 mL of different concentrations of Cr (VI) (20-100 mg/L) at the optimum pH= 2 under shaking at 220 rpm for 24 h. To study the effect of temperature on the adsorption capacity, experiments are carried out by adding 0.02 g of sample to 20 mL of 50 mg/L Cr (VI) at different temperatures (30, 40, 50 and 60 ◦C) at pH = 2.

Absorbance readings of remaining Cr(VI) in solutions have been recorded at triplicate, and the relative standard deviation was < 3%. The experimental data were fitted for linear kinetics and isotherm models with OriginPro 2016 Version 8. One of the most often measured parameters for evaluating the performance of the applied models is the correlation coefficient (R2) detecting the best experimental data with values greater than 0.95.

2.6. Adsorption calculations

To determine the maximum absorbance of each Cr(VI) concentration, 1mL of Cr(VI) solution was put in an indicator acidic solution of 2mL 0.05M H2SO4 and 2mL of 1, 5 diphenylcarbazide dissolved in acetone till a purple-violet color is formed. The maximum absorbance of the Cr(VI)-supernatant solution was analyzed employing a UV-visible spectrophotometer (Type UV-2401PC) in a 1 cm quartz cuvette to check the characteristic absorption peaks of Cr (VI) at a wavelength of 540 nm. The removal percentage (R%) of Cr(VI) ions using samples was amounted by the following equation:

$$R\ \% = \frac{(C_0 - C_e)\ 100}{C_0} \quad (1)$$

The amount of Cr(VI) adsorbed by the solid sample *(qe*, mg/g) was obtained using this equation:

$$q_e = \frac{(C_0 - C_e)\ V}{m} \quad (2)$$

The amount of Cr(VI) adsorbed by the samples at time t (min) was labeled as qt (mg/g) and calculated as follows:

$$q_t = \frac{(C_0 - C_t)\ V}{m} \quad (3)$$

Where *C0*, *C*e and *C*t are the concentrations of Cr(VI) in aqueous solution (mg/L) at initial, equilibrium and definite time (t), respectively. V is the volume of the solution (L) and m is the mass of adsorbent (g).

To evaluate the kinetic studies of Cr (VI) adsorption onto the prepared samples, pseudo-first order and pseudo-second order models were performed. The linear form of pseudo-fist order model is described by Lagergren[28]:

$$log(q_e - q_t) = log\ q_e - \left[\frac{k_1}{2.303}\right] t \quad (4)$$

Pseudo-second order model proposed by Ho and Mckay[29] is given below:

$$\frac{t}{q_t} = \frac{1}{k_2 q_e^2} + \left[\frac{1}{q_e}\right] t \quad (5)$$

Where, *qe* (mg/g) is the amount of adsorbed at equilibrium, while *qt* (mg/g) is the amount of adsorbed at time *t*. While, *k1* (min-1), and *k2* (g/mg.min) are the model constants at equilibrium time (*t*).

For discussing the mechanism of equilibrium Cr(VI) adsorption, the linear form of Langmuir, Freundlich, Temkin and Dubinin-Radushkevich models [30–32] were employed to determine the best equilibrium model.

The Langmuir model describes monolayer adsorption on distinct adsorption sites that are localized homogenously. The linear form of Langmuir model is given as [30]:

$$\frac{C_e}{q_e} = \frac{1}{K_L \cdot q_L} + \frac{C_e}{q_L} \quad (6)$$

Where qL (mg/ g) is the maximum adsorption of Cr(VI) and KL (L/g) is the Langmuir adsorption equilibrium constant. Values of qL and KL constants are calculated from the slope and intercept of the isotherm plot Ce/qe vs. Ce.

A dimensionless separation factor (RL) was calculated from the following equation:

$$R_L = \frac{1}{1 + C_o K_L} \quad (7)$$

RL can show if the adsorption process is either irreversible (RL= 0), favorable (0 <RL<1), linear (RL= 1) or unfavorable isotherm (RL>1).

Freundlich isotherm as an empirical model describes the multilayer and heterogeneous adsorption on the adsorbent's surface[31] and its linear form represented in the following equation:

$$\log qe = \log KF + 1/n \log Ce \quad (8)$$

Where, KF (mg/g (L/mg)1/n) is generally an indicator of the adsorption capacity and 1/n is the adsorption intensity which can be calculated from the intercept and slope of the linear plot with log qe versus log Ce. Based on values of 1/n, the adsorption

is classified as, a favorable if 1/n is between 0 and 1, (0 < 1/n < 1), irreversible when 1/n is 0 and unfavorable when 1/n is greater than 1, (1/n > 1).

Temkin isotherm model estimates the heat of adsorption and explains the indirect interactions between the solid adsorbent and Cr(VI) within a medium range of concentrations [32]. Linear form of Temkin equation is represented in equation (9):

$$q_e = B \ln K_T + B \ln C_e \quad (9)$$

Where KT (L/g) is the Temkin isotherm constant, B is a constant which relates to heat of adsorption (B =RT/b, R (8.314 J/mol /K) being the universal gas constant, b is the Temkin constant (J/mol) and T (K) is the absolute temperature.

Dubinin-Radushkevich (*D-R*) *isotherm* can be differentiated between physical and chemical *adsorption* of adsorbates[34]. This model assumes that adsorption occurs by the micropore volume filling onto porous samples rather than layer-by-layer adsorption on the pore walls. According to previous study [33], the D-R isotherm can represent three types of the isotherm curves: S-, L- and H-shaped isotherms. The linear form of this model is given as:

$$\ln qe = \ln QDR - KDR\ \varepsilon 2 \quad (10)$$

Where, QDR is the D-R adsorption capacity (mg/g), KDR is the constant related with adsorption energy (mol2k/L2), and ε is the Polanyi potential; ε =RT ln(1+1/Ce), T is the temperature (K), and E is the main free energy of adsorption ($E = \frac{1}{\sqrt{2K_{DR}}}$ (kJ/mol)).

3. Results and discussion

3.1. XRD investigation for the prepared samples

To study the surface modifications of prepared GO and SBA-16 from carbon and silica components of RHA before and after mixing physically with Cu-MOF sample using APTES as a Schiff base cross-linker, XRD, FTIR and SEM tools were employed. Figure 1 illustrates the main crystalline phases obtained in Cu-MOF, GO, Cu-MOF/GO, SBA-16 and Cu-MOF/SBA-16. For Cu-MOF alone, there are a series of peaks at 2-theta of 7.0°, 13.8°, 15.7°, 19.6°, 30.0°, 37.0° 42.5°, 62.5° and 74.0° that related to crystal planes of (2 2 0), (2 2 2), (3 3 3), (4 2 0), (4 2 2), (7 7 3), (8 8 2), (4 4 0) and (5 3 3), respectively (Fig. 1a). These are agree with the JCPDS # 112954 according to previous reported literature [27, 34, 35]. The XRD profile of GO confirmed the structure of reduced graphene oxide as one broad peak appeared at 2-theta of 24.5o that reflects to the (002) plane of hexagonal graphene layers (Fig. 1b) [26, 36]. After loading Cu-MOF to GO surface linked with APTES, slight changes with shifting to higher accounts are occurred in the XRD profile of GO sample. Because of the low Cu-MOF content, small peaks were produced at 2-theta of 17.9o, 26.5o, 28.4o, 30.9o, and 36.5o, which are marked as red rectangle symbols in Fig 1b, demonstrating Cu-MOF intercalation into the GO matrix. For SBA-16, the synthesized SBA-16 showed two broad peaks at 2-theta of 10.5˚ and 23˚ identified by JCPDS # 00-001-0424 [37] relating to amorphous silica structure as SiO4 tetrahedral according to the recent study [22]. However, after loading Cu-MOF with low content to SBA-16, almost a minor increase in the intensity of 2-theta at 23˚, showing that small portions of Cu-MOF linked to SBA-16 during the modification process (Fig. 1c). Thus, due to the low content attached to SBA-16 surface that has the highest total surface area, the XRD characteristic peaks of Cu-MOF were difficult to distinguish.

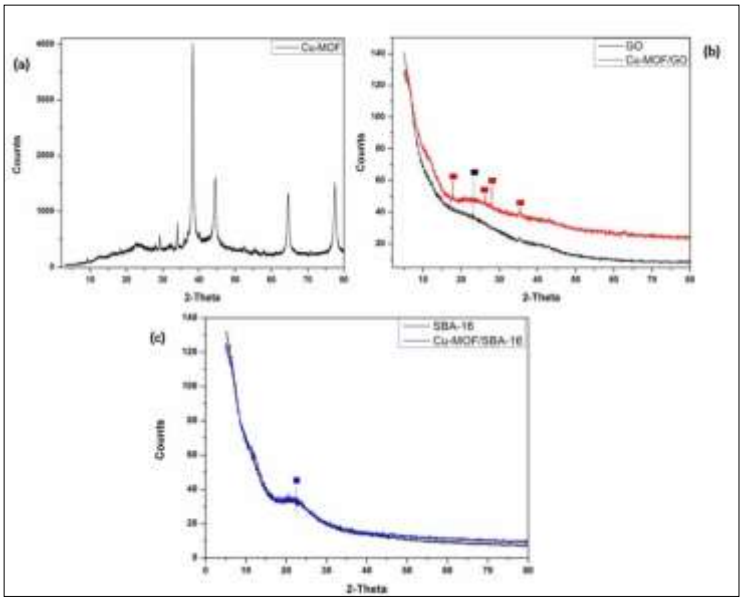

Fig. 1. XRD profiles of the as-prepared (a) Cu-MOF, (b) GO and Cu-MOF/GO and (c) SBA-16 and Cu-MOF/SBA-16.

3.2. Surface groups and morphology analysis

Subsequent to proposed synthesis route, the effective functionalized surfaces of obtained samples using FTIR spectroscopy are depicted in Figure 2. The primary absorption band between 3000-3500 cm-1 signing to the O-H group stretching vibrations can be identified in the FTIR spectra of GO, SBA-16, Cu-MOF, and their composites. The absorption peak of C=O stretching of carbonyl and/or carboxylic moiety functional groups as demonstrated by the GO sheets containing oxygen groups is located at 1711 cm-1 and 1582 cm-1 [26, 36]. This C=O group in GO could permit Cu-MOF to connect to the composite system by either an electrostatic or covalent coupling [38]. The absorption peak at about 1196 cm−1 is ascribed to the C–O stretching vibrations [39]. Additionally, O-H deformation vibration peak is evidenced at 1433 cm-1. For pristine SBA-16, asymmetric high-intensity peak of Si-O at 452 cm-1 is confirmed by the presence of both strong and weak-intensity peaks at 1069 and 970 cm-1, which are attributed to the occurrence of symmetric stretching bands of Si-O-Si and Si-OH, respectively [40]. It is clear from comparing the noticeable peaks for produced pristine Cu-MOF that there is a satisfactory match with the results from earlier research [41, 42]. Its FTIR spectrum shows the characteristic absorption peaks of bending and stretching modes of Cu–O at 488 cm-1 and 721 cm-1 [26, 34], where at 663–766 cm-1 for the absorption peaks related to organic ligand (H2BDC) and sharp peaks with high intensity at 1569 and 1396 cm-1 related to asymmetric and symmetric stretching modes of coordinated carboxylic acid [26, 34]. In addition, two narrow peaks at 2925 and 734 cm-1 attributed to stretching and bending of C–H vibrations in aromatic rings, respectively [22, 34, 43, 44]. The peaks at 970 cm-1, 1500 cm-1 and 1640 cm-1 are ascribed to C=O, C=C and –OH groups of H2BDC, respectively. So, these peaks of the aromatic ring indicate that H2BDC is present in the final product. The sharp absorption peaks between 1385 and 1586 cm-1 showed the in-plane bending vibrations while the stretching vibrations at 675–900 cm-1 of the C=C in the benzene ring [45]. It was determined that the (O-C=O) carboxylate vibration was responsible for the distinctive absorption band at 1655 cm−1 [45]. The vibration of C-O in the precursor was linked to the small peak at 1297 cm-1 [45]. In the Cu-MOF/GO composite, the strength of GO absorption peaks is significantly reduced after loading Cu-MOF, but the absorption peaks of Cu-MOF are not appeared. This result may indicate the occurrence of surface interactions between functional groups of GO and Cu-MOF. There is a somewhat identical in absorption peaks of both Cu-MOF/SBA-16 and SBA-16, affirming low surface loading of Cu-MOF onto SBA-16 surface. However, small peaks at 1440 cm-1 in FTIR spectra of Cu-MOF based composites are observed resulting in the deformation of H-bonded amine groups associated with APTES (i.e., -NH and –NH2) [46].

It is noteworthy to mentioning that the hydrophilic functional groups of both GO and SBA-16 reveal somewhat a hydrophobic nature after loading Cu-MOF through a physical mixing in presence of APTES, as they become less dispersible in water. The FTIR spectra of composites based on Cu-MOF disclose an impressive insertion of a dominant functional group associated with both SBA-16 and GO. This proved that their functional groups and metallic ions in the Cu-MOF structure had stable coordination interactions[38], and their composites were effectively produced [47].

Nonetheless, a significant number of oxygenated functions are still present in the produced composites, which allows them to interact strongly with other materials. The above-mentioned results show that Cu-MOF's low mass ratio (less than 10wt.%) in comparison to SBA-16 and GO may account for the reduced intensity of Cu-MOF's distinctive bands in the generated composites, which is also supported by XRD data. Overall, the presence of hydrophilic groups such as hydroxyl (-OH), carboxylic acid (-COOH), or amino (-NH2) *functional groups* permits significantly the adsorption of Cr(VI).

Furthermore, EDX analysis was used to detect the elements of both Cu-MOF/GO and Cu-MOF/SBA-16, as well as Cu-MOF/GO after Cr(VI) adsorption. Figure 3 depicts the corresponding EDX spectra and the % weight of elements in a specific location of the tested samples. There are five basically elements such as C, N, O, Si, and C, which are related to the chemical compositions of GO, APTES cross-linker and SBA-16 samples employed in this work. Cu-MOF intercalation (0.64%) into the surface SBA-16 samples using APTES cross-linker is extremely minimal in SBA-16 sample, but is slightly large on GO surface (2.37%), confirming that there were no major alterations in the crystal phases or functional surface groups that matched with XRD and FTIR results. After adsorption Cr(VI) on Cu-MOF/GO, EDX spectrum shows the presence of Cr(VI) at a high content of ~ 20.3% with a considerable reduction in the amount of O (36.2%) and Cu (46.8%) suggesting the adsorption of Cr(VI) occurs over O-containing functional groups as well as at Cu-MOF's active sites.

Furthermore, the surface morphology of the as-prepared samples is presented using FE-SEM in Figure 4 (a-f). The prepared reduced GO reveals the successful exfoliation of activated carbon derived from carbon content of rice husk ashless containing randomly stacked and thick platelets of graphene with irregular edges wrinkled surfaces and folding as a result of reduction of graphene sheets (Fig. 4a). SEM image of SBA-16 (Fig. 4b) discloses aggregated spherical-like particles. On the other hand, SEM image of the as-prepared Cu-MOF represents the formation of long and irregular rods- shape (Fig. 4c). Certainly according to above-mentioned results, the combination of GO with Cu-MOF particles is occurred as shown in Fig. 4d. On the other hand, slight change on the surface of Cu-MOF/SBA-16 is observed however, most of Cu-MOF particles diffused into the mesopores of SBA-16 and reduced the total surface area considerably (Fig. 4e). In addition, Fig. 4f represents the SEM micrograph of Cu-MOF/GO after adsorbing Cr(VI), Cr(VI) species as white spots are detected confirming the adsorption of Cr(VI) on the surface of this sample.

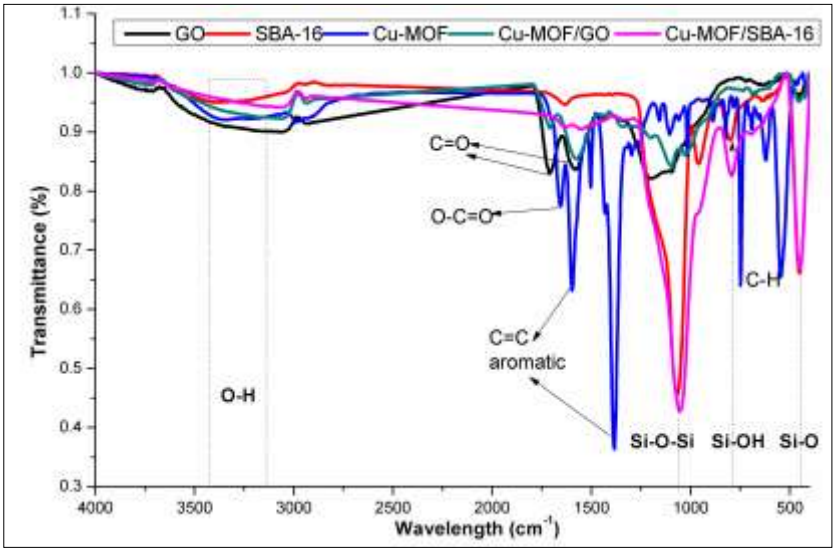

Fig. 2. FTIR spectra of the as-prepared samples

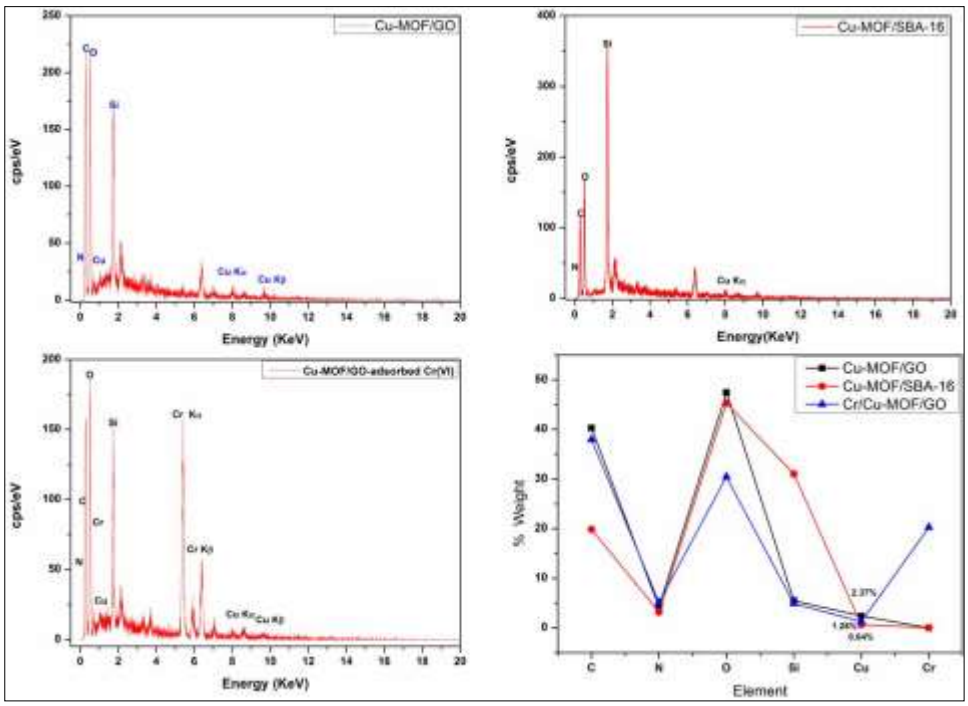

Fig. 3. EDX spectra and % weight of elements in the samples.

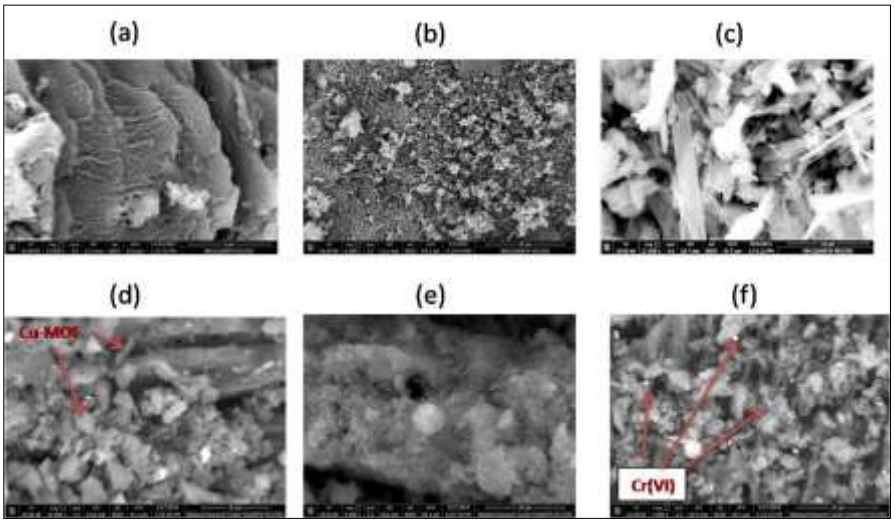

Fig. 4. FE-SEM micrographs of (a) GO, (b) SBA-16, (c) Cu-MOF, (d) Cu-MOF/GO, (e) Cu-MOF/SBA-16 and (f) Cu-MOF/GO-adsorbed Cr (VI)

3.3. Textural measurements

Textural property determination is one of the most common surface characterizations used in this work to highlight the change in porosity caused by mechanical mixing of Cu-MOF with GO and SBA-16 produced from rice husk ashes. By using N2 analysis, the textural properties of GO, SBA-16, Cu-MOF, and their composites are explored. Figure 5 depicts the N2 isotherms of all the prepared samples showing a difference in the isotherm shape. Type I isotherm is obtained in GO, Cu-MOF, Cu-MOF/GO and Cu-MOF/SBA-16 which is a typical of microporous structure with the presence some of mesopores due to existence of desorption branch at P/Po> 0.5. For GO, the obtained N2 isotherm shows a hysteresis loop of H4, referring to the formation of slit-shaped pores with narrow mesopores. On the other side, SBA-16 sample exhibits a IV isotherm type accompanied with a hysteresis loop of H2 type confirming its mesoporous structure and the presence of ink bottle-shaped pore as a result of multilayer adsorption followed by pore condensation in terms of adsorption behaviour [48]. Table 1 tracks the porosity features of the samples calculated from the N2 isotherms. The total surface area (SBET) of GO, SBA-16, Cu-MOF, Cu-MOF/GO, and Cu-MOF/SBA-16 are found to be 195, 484, 36, 23 and 49 m2/g, respectively. As illustrated, the prepared MOF-based samples (Cu-MOF, Cu-MOF/GO, and Cu-MOF/SBA-16) exhibit a lower total surface area than both GO and SBA-16 samples. Additionally, Table 1 demonstrates that the values of total surface area and total pore volume significantly rise when the mean pore diameters decrease. Contrarily, the mean pore diameter greatly expanded after loading Cu-MOF to GO and SBA-16 which is followed by a sharp decline in the total surface area and total pore volume. It can also be deduced that Cu-MOF particles entered and occupied the pores of GO and SBA-16 samples, resulting in a decrease in total surface area and total pore volume. This finding concludes that the mechanical mixing of GO and SBA-16 with low content of Cu-MOF give rises to decreasing the total porosity but with no change in the crystal structure of either GO or SBA-16 samples.

Figure 6 shows the pore size distributions of the prepared samples according to NLDFT model [49]. The samples reveal dominant unimodal peaks of PSDs with different pore widths ranged from 1.3 to 10.3 nm. For Cu-MOF, the maximal pore width was 4.7 nm which is higher than that for GO and SBA-16. After mixing, the maximal pore width was increased considerably to 10.3 and 9.7 nm for Cu-MOF/GO and Cu-MOF/SBA-16, respectively. Accordingly, the combination of Cu-MOF with GO and SBA-16 can improve the pore size distributions which could enhance the adsorption of Cr(VI) onto their surfaces.

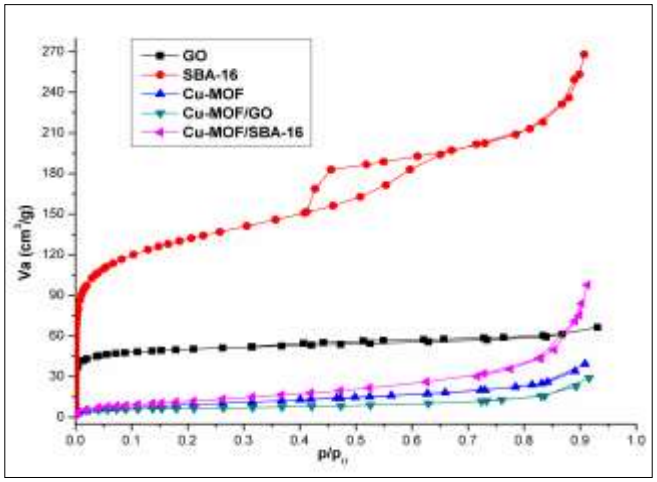

Fig. 5. N_2 adsorption–desorption measurements of prepared samples

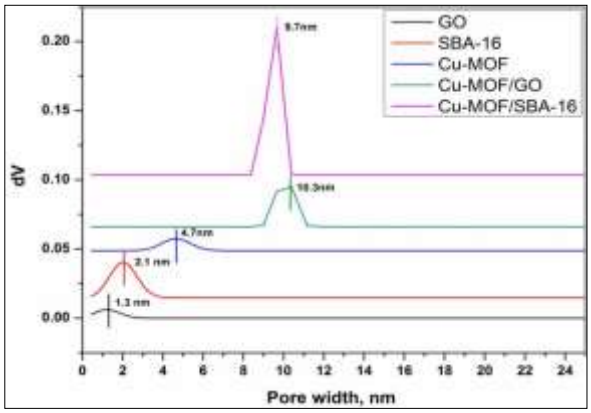

Fig. 6. Pore size distributions in the prepared samples using NLDFT model

3.4. Effect of pH and Cr(VI) initial concentrations

Cr(VI) adsorption is significantly influenced by the pH solution and initial concentrations of Cr (VI) in their aqueous solutions, in addition to the surface properties of the prepared adsorbents. As well, the surface pH of tested samples as listed in Table 1, is almost acidic pH which varied between 3.9 and 5.6, thus the surface of samples is acidic in nature confirming that most of oxygen-containing groups are acidic. Among these, representative samples such as GO, Cu-MOF/GO and Cu-MOF/SBA-16 were selected to determine the best working pH by adjusting the solution pH from 2 to 5. Figure 7 (a) revealed that the adsorption efficiency of Cr(VI) on the tested samples decreases with the increasing pH from 2 to 5. The highest adsorption efficiency of 96.4, 95 and 65% by GO, Cu-MOF/GO and Cu-MOF/SBA-16, respectively, was obtained at pH 2. This result may be attributed to that at pH 2, the surface became increasingly positively charged when the amine and carboxylate groups are protonated, e.g., NH4+ or COOH2+; and thus they become more attractive to the anionic species of Cr(VI) [12, 13, 50, 51]. At acidic pH, Cr(VI) ions mainly existed in the HCrO4– forms, which thus had strong electrostatic attractions on positively charged samples. Hence, adsorption of Cr(VI) is at pH 2 is larger than that in slight acidic pH 5. Furthermore, the surface charge of samples will be turned to negative under alkaline conditions, which decreased the electrostatic attractions and might potentially switch to repulsion between negative charges on the samples and negatively charged CrO42-. Thus the adsorption mechanism of Cr(VI) on the samples maybe governed by surface accommodation at pores and chemical adsorption processes [50-52]. Thus, H-bonding interactions, electrostatic forces, and Van der Waals forces can be used to describe the chemisorption process [51].

The impact of Cr(VI) initial concentrations on the removal efficiency of the prepared samples is illustrated in Figure 7 (b). By increasing the Cr(VI) initial concentration from 20 to 120 mg/L, a substantial decrease in the removal efficiency of all samples is observed. Thus the higher removal efficiencies were 95, 94, 80, 75 and 40% for GO, Cu-MOF/GO, Cu-MOF/SBA-16, Cu-MOF and SBA-16, respectively; at 20 mg/L of Cr(VI), 25 oC, 2 h and pH 2. This result confirms that the accessible surface of adsorbent to initial Cr(VI) concentration ratio is bigger at low Cr (VI) concentrations, resulting in a maximal binding adsorption sites. On the other side, at high Cr(VI) concentrations, the binding sites become saturated and the amount of adsorbent remains constant, leading to a reduction in the adsorption process [54]. The results disclose that the obtained Cu-MOF/SBA-16 sample has a higher adsorption efficiency of Cr(VI) than that of Cu-MOF and SBA-16 individuals while GO sample has a superior adsorption efficiency than its Cu-MOF based composites.

Figure 8 (a and b) demonstrates the removal efficiency of Cr(VI) ions in relation to both porosity (SBET, m2/g) and pH surface of sample adsorbent (pHSlurry) to explain which is more influencer. The SBET factor of each sample shows irregular changes with the removal efficiency of Cr(VI) ions (Fig. 8a) where the decreasing order of this factor as shown: SBA-16 > GO > Cu-MOF/GO > Cu-MOF >Cu-MOF/SBA-16 which results in increasing the removal efficiency in the following order: GO > Cu-MOF/GO > Cu-MOF/SBA-16 > Cu-MOF > SBA-16. Thus the total porosity does not considerably control the removal of Cr(VI) ions. In contrast to SBET, pH surface of samples (Fig.8b) implies its significant role on the removal of Cr(VI) ions, as the pH surface of adsorbents decreases the removal efficiency of Cr(VI). This finding indicates that the adsorbent surface possessing higher acidic oxygen-containing functional groups is very suited to uptake the larger amounts of Cr(VI) through electrostatic interactions as explained above in the effect of solution pH. Therefore, the obtained GO, Cu-MOF/GO, Cu-MOF/SBA-16 samples showed the best Cr(VI) removal based on quantity of acidic oxygen functional groups adhered to their surfaces. Therefore, the presence of acidic functional groups could enhance and control the Cr(VI) adsorption capacity more than the total surface area in the following order; GO> Cu-MOF/GO> Cu-MOF/SBA-16 > Cu-MOF> SBA-16 adsorbents at pH 2.

Table 1. Textural properties of the as-prepared samples

Samples	pH_{Slurry}	S_{BET}, m^2/g	V_P, cm^3/g	R_P, nm
GO	3.9	195	0.103	**2.1**
SBA-16	5.6	484	0.415	**3.4**
Cu-MOF	4.9	36	0.060	**6.7**
Cu-MOF/GO	4.5	23	0.040	**7.8**
Cu-MOF/SBA-16	4.3	49	0.150	**12.3**

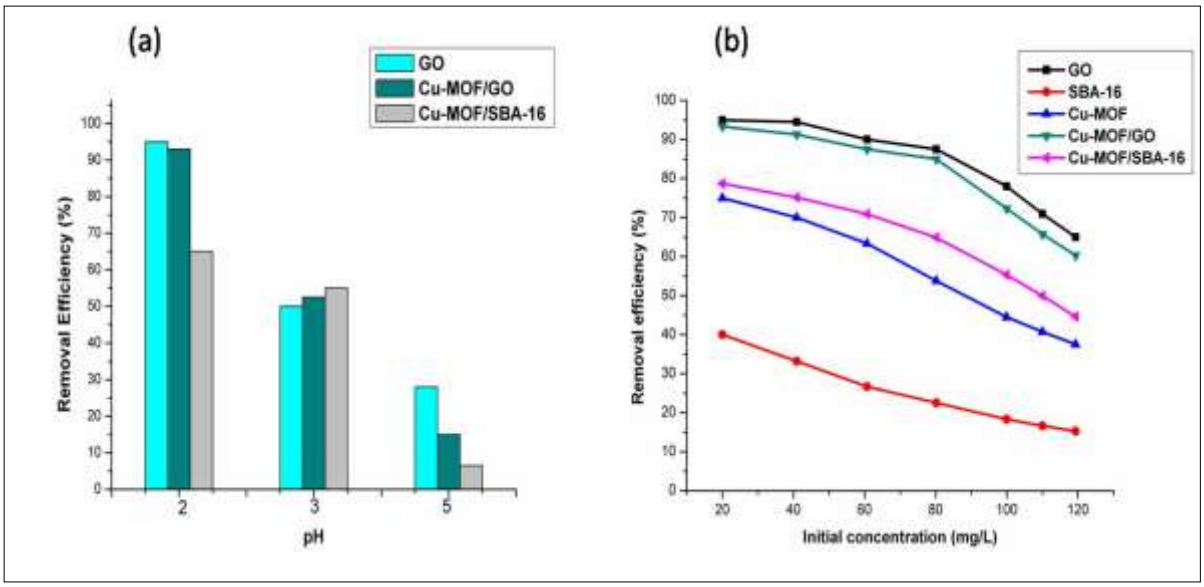

Fig. 7. (a) Effect of pH on adsorption of Cr(VI) ions using the tested samples (C_o=50 mg/L, adsorbent dose=1g/L, V= 20 mL, Time= 2h and T=25ºC)and (b) Effect of Cr(VI) initial concentrations on removal efficiency at pH = 2 (C_o=50 mg/L, adsorbent dose=1g/L, V= 20mL, Time= 2h and T=25ºC)

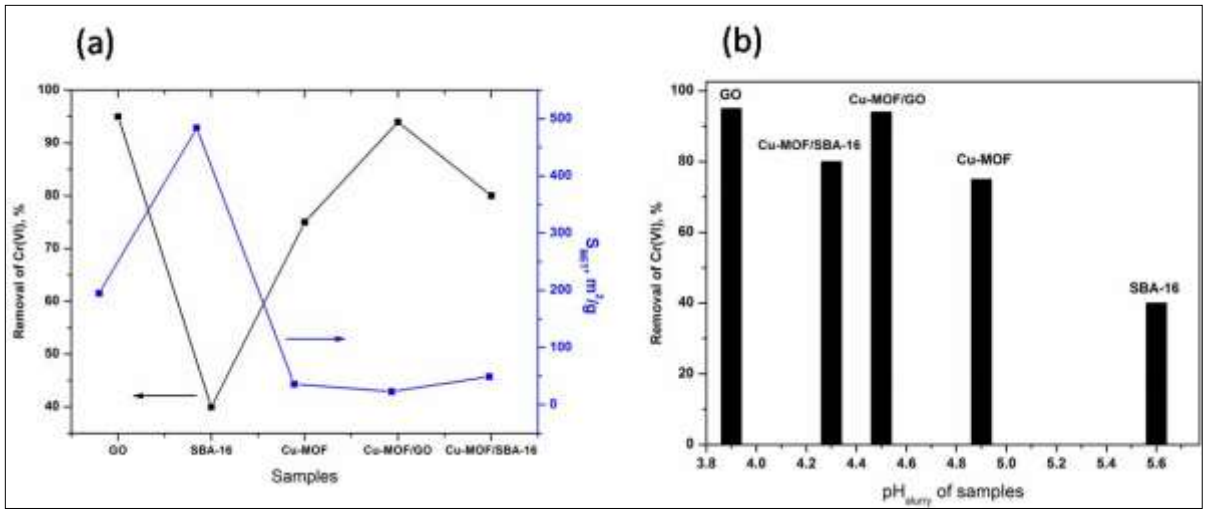

Figure 8. Correlation between removal efficiency of Cr(VI) with (a) total surface area (S_{BET}, m^2/g) and (b) pH of samples' surface(C_o=20 mg/L, adsorbent dose=1g/L, V= 20 mL, Time= 2h, pH 2 and T=25ºC)

3.5. Kinetic adsorption studies

Two well-known pseudo-first-order and pseudo-second-order models were used to analyze the adsorption kinetics of Cr(VI) by all produced materials, as shown in Figure 9. The results of these models are shown in Table 2. Interestingly, the linear plots of two models provide reasonable fitting results according to the correlation coefficients (R2 ≈0.966−0.998). However, the calculated value of qe (Table 2) for the pseudo-first order model is closer to the experimental qe value compared to that of pseudo-second order model; therefore, pseudo-first order model can describe the adsorption of Cr(VI) over all studied samples.

3.6. Equilibrium adsorption studies

The Cr(VI) adsorption behaviour over the adsorbents was investigated by fitting the adsorption isotherm data for Cr(VI) uptake at varied concentrations of 20-120 mg/g applying four models such as Langmuir, Freundlich, Temkin, and D-R isotherms. The adsorption isotherms of Cr(VI) onto the samples are illustrated in Figure 10 (a). The corresponded linear plots of Langmuir models are depicted in Figure 10 (b). Table 3 contains the resulting adsorption parameters of the used models. Obviously, Fig.10a discloses that the adsorption of Cr(VI) is a Langmuir-type adsorption isotherm. Moreover, Langmuir model showed favorable correlation coefficients (R2) of the highest values of R2≈0.989−0.996 then followed by that of Temkin isotherm. The calculated adsorption capacities of samples (qL, mg/g) were found to be 86.1, 22.7, 50, 77 and 66.7 mg/g for GO, SBA-16, Cu-MOF, Cu-MOF/GO and Cu-MOF/SBA-16, respectively. Because GO, Cu-MOF/GO, and Cu-MOF/SBA-16 samples have a higher concentration of acidic surface moieties, they have a greater adsorption capacity. This may attribute to a strong binding interaction between anions of Cr (VI) and positively charged functional groups with Lewis acid character on the surface of these materials.

Furthermore, the calculated RL values were less than 1, and thus the adsorption of Cr(VI) is a proper and reversible on the studied adsorbents. The bT constant calculated from Temkin model can be stated the adsorption mechanism. When the value of bT constant is < 80 kJ/mole [55], the adsorption of Cr(VI) involves a physisorption. Furthermore, the resulted values of bT constant were found to be < 80 kJ/mole, affirming that the Cr(VI) adsorption process onto the studied samples is a physical process. Adsorption is categorized as favorable if 1/n is between 0 and 1 (0 < 1/n < 1), irreversible if 1/n is 0, and unfavorable if 1/n is larger than 1 (1/n > 1) based on values of 1/n taken into account using the Freundlich model. The 1/n values were less than 1, confirming that the adsorption of Cr(VI) is favored by the obtained adsorbents.

Table 4 collects the adsorption capacities for a variety of adsorbents used for removal of Cr(VI) under different conditions. The results in this table manifest that the adsorption capacity of Cr(VI) using prepared samples in this study is suitable and comparable to the other reported adsorbents in literature. The adsorption of Cr(VI) by SBA-16 and Cu-MOF/SBA-16 is not reported yet in the literature.

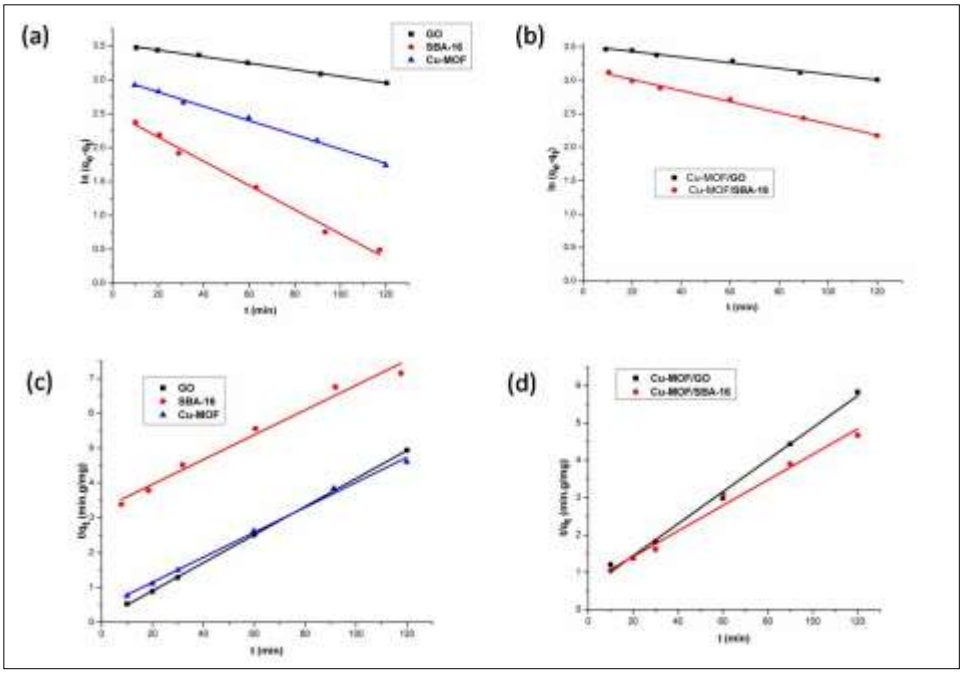

Fig. 9. Linear kinetic plots of (a, b) pseudo first-order and (c, d) pseudo second-order kinetic models for prepared samples

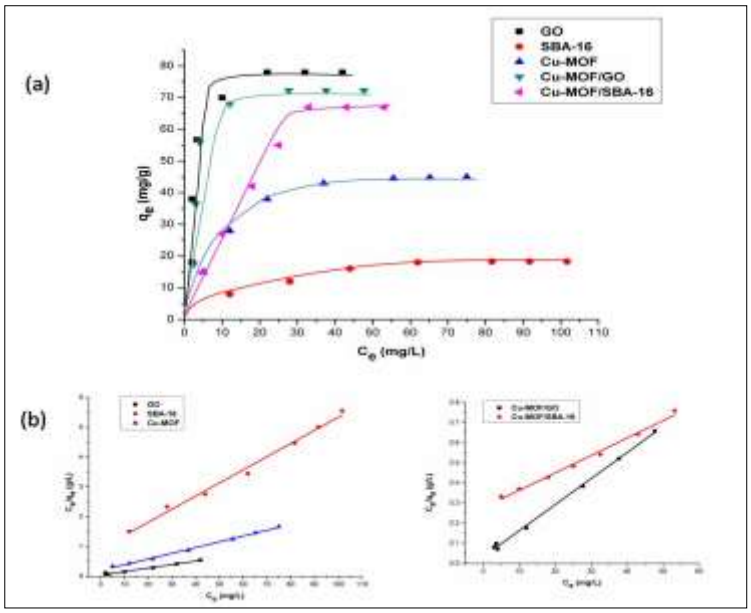

Fig. 10. (a) Adsorption isotherms of Cr(VI) and their corresponded (b) linear plots of Langmuir isotherm

4. Conclusions

Mechanically mixing of GO and SBA-16 with low Cu-MOF content in presence of APTES (~10 wt.%) led to reduction in both the total porosity and hydrophilicity nature but does not affect the crystal structure of either GO or SBA-16 sample. Enhanced uptake capacity of Cr(VI) by the prepared composites was obtained due to the presence of more metal-binding acidic functional groups (e.g., COOH, -OH and –NH2) on its surface. Kinetic data emphasized that the adsorption of Cr(VI) obeys the pseudo-first order goodly. Both Langmuir and Temkin models well described the Cr(VI) adsorption better than other models. The superior adsorption capacity of GO, SBA-16, Cu-MOF, Cu-MOF/GO and Cu-MOF/SBA-16 (66.7-86.1 mg/g) attributed to their high concentrations of acidic functional groups. Such groups can provide additional adsorption sites that favor the adsorption of chromium (VI) anions formed at pH 2. The adsorption mechanism of Cr(VI) on the samples maybe governed by surface accommodation at pores and physical adsorption processes. Overall, the current study reveals the potential utility of rice husk ashes to fabricate GO, SBA-16 and Cu-MOF composites as novel Cr(VI)-adsorbents that would make them have potential applications in wastewater purification, adsorption, gas separation, and molecular sieving membranes.

Table 2. Kinetic constants for Cr (VI) removal of Co= 50 mg/L and pH 2 by prepared samples

		Pseudo-first order model			**Pseudo-second order model**		
Kinetic parameters	$q_{e(exp)}$ **(mg/g)**	k_1 **(min^{-1})**	q_e **(mg/g)**	R^2	k_2 **(**g/mg.min**)**	q_e **(mg/g)**	R^2
GO	38	0.005	34.5	0.9979	0.012	25	0.9809
SBA-16	12	0.018	12.5	0.991	0.0004	27.4	0.9658
Cu-MOF	28	0.01	27.1	0.9952	0.0036	26	0.9957
Cu-MOF/GO	36.5	0.004	34	0.9854	0.002	26.6	0.9681
Cu-MOF/SBA-16	27	0.008	24.3	0.9936	0.0016	33	0.9827

Table 3. Calculated parameters of the studied isotherms for adsorption of Cr(VI).

	Langmuir isotherm approach				Freundlich isotherm approach		
Adsorbent	**q_L (mg/g)**	**K_L (L/mg)**	**R_L**	**R^2**	**K_F** (mg/g $(L/mg)^{1/n}$)	**1/n**	**R^2**
GO	86.1	0.3	0.14	0.991	20.7	0.41	0.771
SBA-16	22.7	0.05	0.5	0.989	3.2	0.39	0.930
Cu-MOF	50	0.1	0.33	0.995	9.6	0.38	0.871
Cu-MOF/GO	77	0.4	0.11	0.996	25.6	0.29	0.898
Cu-MOF/SBA-16	66.7	0.054	0.48	0.989	6	0.668	0.949
	Dubinin–Radushkevich isotherm approach				**Temkin isotherm approach**		
	q_{DR} (mg/g)	**K_{DR} (mol^2/Jol^2)**	**E(K.J/mol)**	**R^2**	**b_T (K.J/mol)**	**K_T (L/mg)**	**R^2**
GO	79	$1.1x10^{-6}$	0.666	0.800	0.175	8.6	0.951
SBA-16	17.6	$2.1x10^{-5}$	0.154	0.871	0.48	0.4	0.947
Cu-MOF	42.5	$5.3x10^{-6}$	0.30	0.899	0.222	1	0.936
Cu-MOF/GO	76.4	$1.8x10^{-6}$	0.50	0.897	0.15	2.2	0.93
Cu-MOF/SBA-16	58.6	$7.3x10^{-6}$	0.25	0.836	0.10	0.4	0.95

Table 4. Maximum adsorption capacities (q_L, mg/g) reported in the literature for Cr (VI) adsorption.

Adsorbent	q_L (mg/g)	Reference
GO	86.1	This work
SBA-16	22.7	This work
Cu-MOF	50	This work
Cu-MOF/GO	77	This work
Cu-MOF/SBA-16	66.7	This work
Cu(II)-MOF	190	[16]
Si @ activated carbon	268	[11]
Mesoporous activated carbon	30.3	[12]
Carbon nanostructures	56	[13]
Cu(II)-MOF	190	[16]
Graphene oxide	1.22	[56]
SBA-15-NH_2	52.1	[57]

Acknowledgments
The authors would like to thank the National Research Centre in Egypt for financial support under project #13020219.

Conflict of interests
The authors declare no competing interest.

Funding
There is no financial funding from the institute.

Data Availability Statement
All data are available on request.

References
[1] A. Noor and S.A. Khan, Sustain **15**, 4246 (2023).
[2] S.M. El-Khouly and N.A. Fathy, Egypt J Chem **64**, 7029 (2021).
[3] N. Kazakis, N. Kantiranis, K. Kalaitzidou, M. Kaprara, M. Mitrakas, R. Frei, G. Vargemezis, P. Tsourlos, A. Zouboulis, and A. Filippidis, Sci Total Environ **593**–**594**, 552 (2017).
[4] R.T. Achmad, Budiawan, and E.I. Auerkari, Annu Res Rev Biol **13**, 1 (2017).
[5] E. Vaiopoulou and P. Gikas, Chemosphere **254**, 126876 (2020).
[6] M. Tumolo, V. Ancona, D. De Paola, D. Losacco, C. Campanale, C. Massarelli, and V.F. Uricchio, Int J Environ Res Public Health **17**, 1 (2020).
[7] S. Naghdi, M.M. Shahrestani, M. Zendehbad, H. Djahaniani, H. Kazemian, and D. Eder, J Hazard Mater **442**, 130127 (2023).
[8] P. Sharma, S.P. Singh, S.K. Parakh, and Y.W. Tong, Bioengineered **13**, 4923 (2022).
[9] R. Jobby, P. Jha, A.K. Yadav, and N. Desai, Chemosphere **207**, 255 (2018).
[10] M.A. Islam, M.J. Angove, and D.W. Morton, Environ Nanotechnology, Monit Manag **12**, 100267 (2019).
[11] G.M. Mohamed, S.A.S. Ahmed, and N.A. Fathy, Chem Africa **6**, 3097 (2023).
[12] N.S. Ammar, N.A. Fathy, H.S. Ibrahim, and S.M. Mousa, Appl Water Sci **11**, 1 (2021).
[13] N.A. Fathy, S.M. El-Khouly, and O.I. El-Shafey, Curr Anal Chem **17**, 975 (2021).
[14] M.R. Adam, N.M. Salleh, M.H.D. Othman, T. Matsuura, M.H. Ali, M.H. Puteh, A.F. Ismail, M.A. Rahman, and J. Jaafar, J Environ Manage **224**, 252 (2018).
[15] D. Yuan, C. Shang, J. Cui, W. Zhang, and Y. Kou, Environmental Research **216**, 114616 (2023).
[16] Z. Shao, C. Huang, Q. Wu, Y. Zhao, W. Xu, Y. Liu, J. Dang, H. Hou, J. Hazardous Materials **378**, 120719 (2019).
[17] P. Liang, S. Liu, M. Li, W. Xiong, X. Yao, T. Xing, and K. Tian, Sep Purif Technol **336**, 126222 (2014).
[18] D. Yuan, C. Shang, J. Cui, W. Zhang, and Y. Kou, Environ Res **216**, (2023).
[19] S.K. Sharma, G. Sharma, A. Sharma, K. Bhardwaj, K. Preeti, K. Singh, A. Kumar, V.K. Pal, E.H. Choi, S.P. Singh, and N.K. Kaushik, Appl Surf Sci Adv **8**, 100225 (2022).
[20] T.H. Liou, S.Y. Wang, Y.T. Lin, and S. Yang, Colloids Surfaces A Physicochem Eng Asp **636**, 128150 (2022).
[21] H.A.G. Bazani, A. Thomé, R.F. Affeldt, and L.F.D. Probst, New J Chem **46**, 7899 (2022).
[22] S.S. El-Shafey, S.A.S. Ahmed, R.M. Aboelenin, and N.A. Fathy, Desalin Water Treat 317 (2024) 100179.
[23] Y. Cheng, M. Lu, J. Li, X. Su, S. Pan, C. Jiao, and M. Feng, J Colloid Interface Sci **369**, 388 (2012).
[24] T.H. Liou and P.Y. Wang, Waste Manag **108**, 51 (2020).
[25] P. Singh, J. Bahadur, and K. Pal, Graphene **06**, 61 (2017).
[26] N.A. Fathy, S.A. Sayed Ahmed, R.M. Aboelenin, and Shaimaa S. El - Shafey, New J Chem 48, 7726 (2024).
[27] A.S. Abdelmoaty, A.A. El-Beih, and Adli A. Hanna Synthesis, J Inorg Organomet Polym Mater **32**, 1778 (2022).
[28] S. Lagergren, Handlingar **24**, 1 (1898).
[29] Y.S. Ho and G. McKay, Chem Eng J **70**, 115 (1998).
[30] I. Langmuir, Am Chem Soc **40**, 1361 (1918).
[31] H.M.. Freundlich, J Phy Chem **57**, 385 (1906).
[32] M. Temkin and V. Pyzhev, Acta Physicochim URSS **12**, 327 (1940).
[33] M.M. Dubinin, E.D. Zaverina, and L. V. Radushkevich, ZhurnalFizicheskoiKhimii **21**, 1351 (1947).
[34] Q. Hu and Z. Zhang, J Mol Liq **277**, 646 (2019).
[35] A.R. Bagheri and M. Ghaedi, Arab J Chem **13**, 5218 (2020).
[36] M. Zhong, S. Zhang, A. Dong, Z. Sui, L. Feng, and Q. Chen, J Mater Sci **55**, 10388 (2020).
[37] M. Rosillo-Lopez and C.G. Salzmann, Carbon N Y **106**, 56 (2016).
[38] W.J.J. Stevens, K. Lebeau, M. Mertens, G. Van Tendeloo, P. Cool, and E.F. Vansant, J Phys Chem B **110**, 9183 (2006).
[39] S. Luo and J. Wang, Env Sci Pollut Res **25**, 5521 (2018).
[40] Z. Çiplak, N. Yildiz, and A. Cąlimli, Fullerenes Nanotub Carbon Nanostructures **23**, 361 (2015).
[41] K.M. Abas and N.A. Fathy, Int J Environ Sci Technol **November**, 1 (2023).
[42] S. John, B. Mathew, E.P. Koshy, and C. George, Mater Today Proc **25**, 230 (2019).
[43] E.D. Dikio and A.M. Farah, Chem Sci Trans **2**, 1386 (2013).
[44] N.E. Tari, A. Tadjarodi, J. Tamnanloo, and S. Fatemi, J CO2 Util **14**, 126 (2016).
[45] A.H. Shah, Z.U. Abideen, S. Maqsood, F. Rashid, R. Ullah, A.U. Rehman, M. Dildar, M. Ahmad, K. Ullah, M.N. Rafi, and F. Teng, J Solid State Chem **322**, 123935 (2023).
[46] H. Yarahmadi, S.K. Salamah, and M. Kheimi, Sci Rep **13**, 19136 (2023).

[47] J. Pokhrel, N. Bhoria, S. Anastasiou, T. Tsoufis, D. Gournis, G. Romanos, and G.N. Karanikolos, Microporous Mesoporous Mater **267**, 53 (2018).
[48] A. Taufiq, A. Nikmah, A. Hidayat, S. Sunaryono, N. Mufti, N. Hidayat, and H. Susanto, Heliyon **6**, (2020).
[49] K. B, Esrafili A, M.-B. A, J. AJ, and K. RR, Water Sci Technol **69**, 147 (2014).
[50] G. Kupgan, T.P. Liyana-Arachchi, and C.M. Colina, Langmuir **33**, 11138 (2017).
[51] I. Hussain, J. Qi, X. Sun, L. Wang, and J. Li, J Mol Liq **318**, 114052 (2020).
[52] F. Chen, S. Guo, Y. Wang, L. Ma, B. Li, Z. Song, L. Huang, and W. Zhang, Front Environ Sci Eng **16**, 1 (2022).
[53] G. Gebrehawaria, A. Hussen, and V.M. Rao, Int J Environ Sci Technol **12**, 1569 (2015).
[54] G.M. Mohamed, W.E. Rashwan, N.A. Fathy, and S.A. Sayed Ahmed, Desalin Water Treat **148**, 178 (2019).
[55] Y. Wu, S. Zhang, X. Guo, and H. Huang, Bioresour. Technol. **99**, 7709 (2008).
[56] N.K. Mondal, and S. Chakraborty, Appl Water Sci **10**, 61 (2020).
[57] J.M. Yoo, S.S. Park, Y.Z. Yan, C.S. Ha, Materials (Basel) **14**, 5060 (2021).